


## Article

# Effects of Chemical Short-Range Order and Lattice Distortion on Crack-Tip Behavior of Medium-Entropy Alloy by Atomistic Simulations

Xiuju Zhu <sup>1,2</sup>, Fuhua Cao <sup>3,\*</sup>, Lanhong Dai <sup>1,2</sup>  and Yan Chen <sup>1,2,\*</sup>

<sup>1</sup> State Key Laboratory of Nonlinear Mechanics, Institute of Mechanics, Chinese Academy of Sciences, Beijing 100190, China

<sup>2</sup> School of Engineering Science, University of Chinese Academy of Sciences, Beijing 101408, China

<sup>3</sup> School of Materials Science and Engineering, Central South University, Changsha 410083, China

\* Correspondence: caofuhua@csu.edu.cn (F.C.); chenyan@lnm.imech.ac.cn (Y.C.)

**Abstract:** It is well demonstrated that the complex chemical fluctuations on high/medium-entropy alloys (H/MEAs) play critical roles in their deformation process, but there are few reports related to the effect of such complex chemical fluctuations on the crack behavior. In this paper, the effects of chemical short-range order (CSRO) and lattice distortion (LD) on the crack-tip behavior of CrCoNi MEAs under mode I loading at room temperature are investigated by carrying out molecular dynamics (MD) simulation, hybrid MD/Monte-Carlo (MC) simulation and the  $J$ -integral method. The results reveal that CSRO can improve the  $J$ -integral value without significant changes in the localized deformation zone size. On the contrary, LD can lower the  $J$ -integral value with an increase in the localized deformation zone size. The energetic analysis shows that CSRO improves the activation energy barrier of Shockley partial dislocation from the crack-tip while LD reduces the activation energy barrier. Our work is a step forward in understanding the effects of CSRO and LD on the crack-tip behavior and deformation mechanisms of CrCoNi MEAs.

**Keywords:** chemical short-range order; lattice distortion;  $J$ -integral; localized deformation zone; crack; molecular dynamics



**Citation:** Zhu, X.; Cao, F.; Dai, L.; Chen, Y. Effects of Chemical Short-Range Order and Lattice Distortion on Crack-Tip Behavior of Medium-Entropy Alloy by Atomistic Simulations. *Metals* **2024**, *14*, 226. <https://doi.org/10.3390/met14020226>

Academic Editor: Luis Antonio Barrales-Mora

Received: 9 January 2024

Revised: 2 February 2024

Accepted: 10 February 2024

Published: 13 February 2024



**Copyright:** © 2024 by the authors. Licensee MDPI, Basel, Switzerland. This article is an open access article distributed under the terms and conditions of the Creative Commons Attribution (CC BY) license (<https://creativecommons.org/licenses/by/4.0/>).

## 1. Introduction

High-entropy alloys (HEAs), which are composed of multiple principal elements, possess special characteristics including high entropy, chemical short-range order (CSRO) and lattice distortion (LD) [1,2], and they are quite different than traditional alloys usually based on one parent metal. Due to their specific structure, HEAs exhibit excellent properties [1] such as a high strength [3–5], high toughness [6–8], corrosion resistance [9–11], wear resistance [12] (similar with high-alloy coating materials [13]) and outstanding self-sharpening capability [14], which make them promising candidates for applications in various fields. It is widely reported that HEAs with an FCC structure have good ductility and fracture toughness [1] and even excellent mechanical properties at low temperatures [6]. On the basis of the well-studied equimolar Cantor alloy, researchers have developed several related variants with less alloying elements. The most famous example is the equal atomic, medium-entropy alloy (MEA) CrCoNi [15,16]. Gludovatz et al. [7] studied the special damage tolerance of CrCoNi MEA at 77 K by experiments. The results show that CrCoNi is one of the most damage-resistant materials. In order to reveal the underlying origin of the high damage resistance, intense attention has been paid to crack-tip behavior [17–20]. It is revealed that the high fracture toughness is caused by a combination of crack-tip blunting, crack bridging and deflection [20]. Among these, the crack-tip blunting is mainly caused by dislocation emission from the crack-tip, and the emitted dislocation can produce back stress to lead to the shielding effect [21].

The macroscopic mechanical properties of CrCoNi MEA are closely related to its CSRO and LD. CSRO is usually a thermally induced concentration fluctuation, which is directly related to the chemical-pair correlation [22–25]. Due to the diversity of atomic radii, the arrangement of atoms in MEAs is not an ideal disordered state [26–28]. The probability of different or identical atoms meeting each other is high, and chemical interactions occur. Atoms tend to attract or repel each other, that is, neighboring atoms preferentially choose to avoid or aggregate, forming CSRO. Therefore, CSROs are the inherent microstructural properties of MEAs, and the CSRO is clearly observed in the MEAs such as VCoNi [29] and CrCoNi [30]. The degree of CSRO in CrCoNi MEAs has a positive effect on the stacking fault energy [31,32]. The increase in the CSRO degree in MEAs will also alter the dislocation slip path, thereby affecting the interaction and storage of dislocations, ultimately altering the ductility and hardening of MEAs [33,34]. Zhang et al. [35] showed that the deformation behavior of MEAs was directly correlated with the degree of CSRO. Ghosh et al. [36] employed on-lattice machine learning interatomic potentials and canonical Monte-Carlo (MC) simulations to find that magnetism is not the driving force in determining the ground-state ordering in CrCoNi. An LD effect was found in HEAs because of atomic interactions and an atomic size mismatch [37–39]. The degree of LD varies with the types of atomic species in the HEAs [37,38]. Compared with traditional alloys, the local stress field caused by severe LD in HEAs strongly hinders the motion of dislocations [14]. It was revealed that LD lowers the Young's modulus and strain for the nucleation of Shockley partials [38] and leads to a change in the dislocation dissociation width along the dislocation line and relatively high-energy barriers for dislocation motion [40].

The crack-tip field is a bridge to constructing macro- and micro-deformation and fracture of materials. The atomic-scale microstructure evolution around the crack-tip is a key problem in understanding the fracture mechanism of MEAs. However, a precise characterization of a crack-tip by experimental observation is extremely difficult. As a supplement to existing experimental techniques and theories, molecular dynamics (MD) simulation is a powerful tool for studying plastic deformation and fracture behavior in HEAs/MEAs at an atomic-scale [41–44]. The chemical inhomogeneity effects and the atomic- and electronic-level mechanism for grain boundary (GB) deformation and fracture in CrCoNi alloys were investigated by performing MD simulation and first-principle calculation [45]. The effect of the crystal orientation on the crack-tip behavior was numerically studied in single-crystal CrMnFeCoNi HEA [18] and MnFeNi MEA [19]. The  $J$ -integral defined by Rice [46] is an extremely significant parameter in fracture mechanics. The onset of crack growth can be characterized by the critical value of the  $J$ -integral [47]. The validity of the nanoscale application of continuum-based linear elastic fracture mechanics methodology was investigated, and the concept of the continuum  $J$ -integral was extended to the atomistic domain [48]. The atomistic  $J$ -integral approach was used to study the fracture mechanisms and the influences of surface crack on the mechanical properties of silica glass [49]. The effects of the crack length on the mechanical properties of single-crystalline Cantor alloys at 0.1K were revealed by MD simulations combining the  $J$ -integral [50].

Although researchers have carried out numerous studies on the mechanical properties and deformation mechanism of CrCoNi MEA and provided important understandings, the crack-tip behavior and its micro-mechanisms remain elusive. The influence of internal factors (e.g., CSRO and LD) on the crack-tip field still needs further research. In this paper, MEA samples with different degrees of CSRO and LD are built with a pre-existing edge crack, and the crack-tip field behavior and its correlations with the internal CSRO and LD of MEAs under mode I loading at room temperature are investigated by carrying out MD simulation, hybrid MD/MC simulation and the free-end nudged elastic band (FE-NEB) method. The  $J$ -integral and dislocation activation energy are calculated for CrCoNi MEAs with different degrees of CSRO and LD to quantitatively describe the underlying mechanisms.

## 2. Methodology

### 2.1. MD Simulations

To study the effect of CSRO and LD, three rectangular CrCoNi MEA samples with different chemical distributions, namely, MCMD400K, Random and Ave-atom, are built, and a preexisting edge crack is embedded in each sample (Figure 1). To create the MEA with random solid solution structures, Ni atoms in the FCC phase are randomly selected and replaced with Co and Cr until the desired composition is achieved [38]. The average lattice parameter of this alloy is 3.56 Å. The hybrid MC/MD simulations are performed to ensure that the systems are relaxed simultaneously in both chemical and structural freedom [32,51]. During the MC/MD simulation, the 1 MC steps were performed on one-quarter of the atoms with  $\Delta\mu_{\text{Ni-Co}} = 0.021$  eV and  $\Delta\mu_{\text{Ni-Cr}} = -0.31$  eV every 20 MD steps [51]. The Random sample with LD is expected to have no CSRO, as indicated by the nearly zero absolute values of all parameters. The MCMD400K CoCrNi sample, generated at a 400 K annealing temperature, exhibits CSRO that the Random sample does not possess. To help understand the LD effect on crack-tip behavior, the Ave-atom sample is built based on a hypothetical pure average-atom interatomic potential [38,51], bearing the same bulk properties of equal atomic CrCoNi MEA but no LD and CSRO.

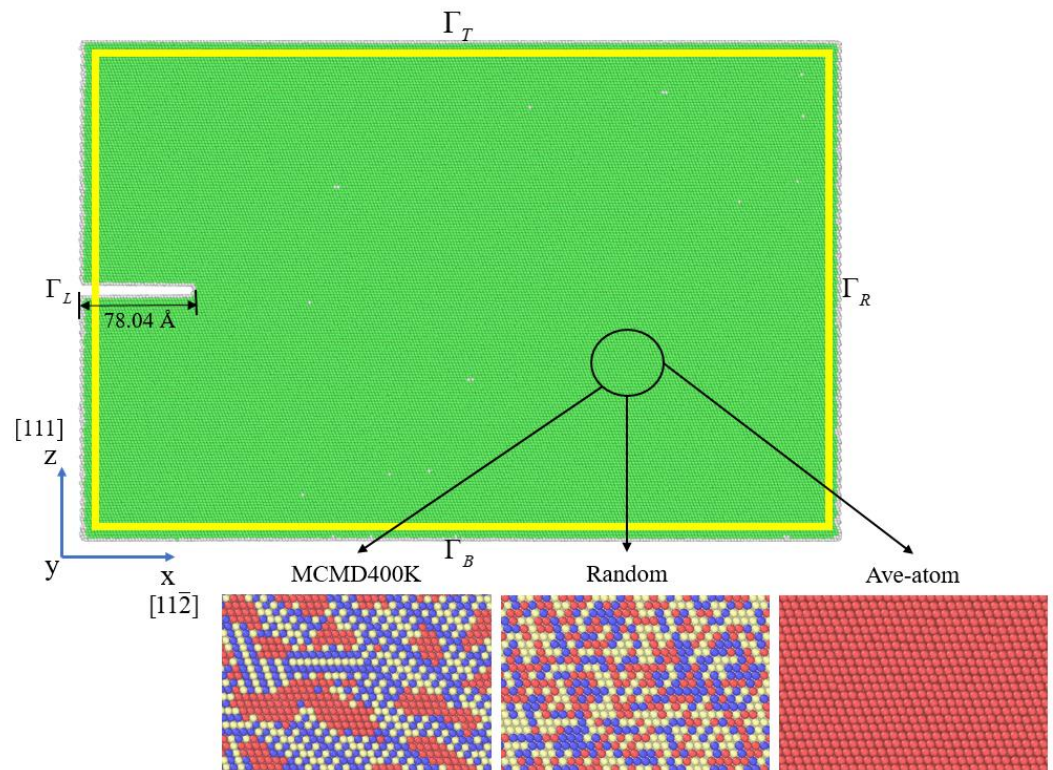


**Figure 1.** Schematic diagram of the simulated configuration and the counterclockwise rectangular  $J$ -integral contour around the crack-tip. In the small images (MCMD400K and Random configurations) below, atoms colored by red, blue and yellow represent Ni, Co and Cr atoms, respectively.

The size of the MEA sample is  $526 \times 30.234 \times 345.60$  Å<sup>3</sup> (about 500,000 atoms) along the X direction-[112], the Y direction-[110] and the Z direction-[111], respectively, where the Z direction is the tensile crystal direction. A pre-crack is introduced by removing a few layers of atoms, resembling the crack cut by the focused ion beam technology in actual experiments. The initial crack length is 78.04 Å, and the average crack opening distance is 6.17 Å. The crack front is parallel to the Y direction and the crack surface is perpendicular to the Z direction. To obtain uniform far field stress and minimize finite width effects, dimensions of the model in the Z direction and X direction are considered much larger than the crack size. In order to avoid the influence of a surface effect on edge

crack propagation, periodic boundary conditions are applied in the Y direction. The free surface is generated in the X direction by introducing a vacuum layer (about 20 Å) to avoid the artificial interaction between the periodic boundary. The non-periodic boundary condition is applied in the Z direction to meet the loading conditions. The temperature of the system is kept at 298 K in all the simulations. A Nose–Hoover thermostat [52,53] is employed to control the constant temperature. The simulations use a time step of 1 fs, and all the configurations are thoroughly relaxed with energy minimization and then equilibrated in an isobaric-isothermal (NPT) ensemble at a temperature of 298 K for 100 ps. After the relaxations, nine layers of atoms are selected as rigid bodies from upper and lower ends, resembling the clamping position in actual uniaxial tensile experiments. The uniaxial tensile loading is applied to the MEA samples for 1000 ps in an NPT ensemble at 298 K and at a constant strain rate of  $1.005 \times 10^8 \text{ s}^{-1}$  by rigidly moving the upper rigid body and fixing the lower rigid body. The open-source MD code LAMMPS (LAMMPS-12 December 2018, Sandia National Laboratories, USA) is used for atomic simulation, and the open visualization tool (OVITO) is used for simulation data post-processing [54].

The choice of interatomic potential is crucial in atomistic simulations. In this work, the interaction between Cr, Co and Ni atoms is simulated within the framework of the Embedded Atom Method (EAM) [32,55]. The recently developed DFT-calibrated embedded-atom potential for CrCoNi MEAs by Li, Sheng and Ma [32] is used. This EAM potential captures typical features of MEAs, i.e., multiple principal components with similar atomic sizes, chemical interactions consistent with typical MEA solutions and single-phase solutions with variable CSRO, and provides a relatively accurate description of stacking fault energy compared with DFT calculations [32]. Furthermore, to create the Ave atom model in this study, the average atomic potential can be fit based on the EAM potential [32]. The machine learning potential for CrCoNi was recently developed and might have potential for high accuracy for simulations of CSRO [36].

## 2.2. Free-End Nudged Elastic Band Estimation

To gain a quantitative characterization of the heterogeneous nucleation mechanism at the crack-tip, the free end adaptive fretted elastic band (FEA-NEB) method [56,57] is used to calculate the MEP of dislocation activation at the crack-tip. FEA-NEB can help solve the convergence problem and locate the transition state to increase the image clarity near the transition state [58].

The minimum energy path calculated by NEB is obtained through the following steps. The atomic configurations with different stress levels in the elastic stage are selected as the initial configuration, and the atomic configurations with a single dislocation ring at the crack-tip are selected as the final atomic configurations. Then, the cg algorithm is used to fully relax the initial and final configurations. Finally, a set of initial configurations are linearly interpolated between the initial and final configurations.

## 2.3. Crack-Tip Field Theory

### 2.3.1. *J*-Integral

According to Rice (1968) [46], a path-independent *J*-integral can be introduced to describe the driving force of the crack-tip field. The proof of path independence is strictly applicable to the path around the crack-tip in elastic materials outside the plastic zone. When the deformation plasticity theory (actually, nonlinear elasticity) is adopted, the path independence result is also applicable to the path passing through the plastic zone. The *J*-integral is expressed as [46]

$$J = \int_{\Gamma} \left( W dz - T_i \frac{\partial u_i}{\partial x} d\Gamma \right) \quad (1)$$

with

$$W = \int_0^\varepsilon \sigma_{ij} d\varepsilon_{ij} \quad (2)$$

where  $W$  is the strain energy,  $T_i$  is the traction force,  $\partial u_i / \partial x$  are the components of the displacement gradient and  $\Gamma$  is the boundary contour. In the discrete MD domain, it is impossible to calculate the line integral strictly, because it is very complicated to define the stress and strain as a line atom by atom, and the atomic stress and strain data fluctuate greatly. Therefore, we need to use a summation of discrete regions to calculate the  $J$ -integral. A rectangular contour along the domain boundaries, as shown in Figure 1, is chosen, which is 5 Å~10 Å away from the boundary [49,50]. In order to prevent a big fluctuation in the results, the  $J$ -integral is calculated by taking the integration path from the distance boundary 5 Å to the distance boundary 10 Å, and then the average value of the results is calculated. The width and length of the discrete area are both set to 5 Å, while the thickness is consistent with the thickness of the model. The discretized zones for the  $J$ -integral contour are depicted in Figure 1. Based on Equation (1), the total  $J$ -integral is expressed as:

$$J = J_{\Gamma_T} + J_{\Gamma_L} + J_{\Gamma_B} + J_{\Gamma_R} \quad (3)$$

where  $\Gamma_T$ ,  $\Gamma_L$ ,  $\Gamma_B$  and  $\Gamma_R$  are the top, left, bottom and right contours.

According to simulation conditions, the model can be considered as a 2D model with the condition of plane stress, and then:

$$W = \frac{1}{2}(\sigma_{xx}\varepsilon_{xx} + \sigma_{zz}\varepsilon_{zz} + \sigma_{xz}\gamma_{xz}) \quad (4)$$

$$T_i \frac{\partial u_i}{\partial x} = T_z \frac{\partial u_z}{\partial x} + T_x \frac{\partial u_x}{\partial x} \quad (5)$$

For the  $\Gamma_L$  and  $\Gamma_R$  contours, traction  $T_i$  is zero due to free surfaces. For the  $\Gamma_T$  and  $\Gamma_B$  contours,  $T_x = 0$  and  $\partial u_z / \partial x = 0$  because the model is stress-free in the X direction and boundaries are uniformly loaded in the Z direction. Therefore, Equation (3) can be expressed as:

$$J = \int_{\Gamma_T} (Wdz) + \int_{\Gamma_L} (Wdz) + \int_{\Gamma_B} (Wdz) + \int_{\Gamma_R} (Wdz) \quad (6)$$

At the  $\Gamma_T$  and  $\Gamma_B$  contours,  $dz = 0$ ; therefore,

$$\int_{\Gamma_T} (Wdz) + \int_{\Gamma_B} (Wdz) = 0 \quad (7)$$

Therefore, the final form of the  $J$ -integral is expressed as:

$$J = \int_{\Gamma_L} (Wdz) + \int_{\Gamma_R} (Wdz) \quad (8)$$

where  $\Gamma_L$  and  $\Gamma_R$  are the left and right contours.

During the calculation, Hardy stress instead of Virial stress is summed up for all atoms inside the discrete region to reduce the fluctuation [49]. The Hardy stress of atom  $i$  is given as [49,50,59]:

$$\sigma^{avg}(i) = \frac{1}{N} \sum_{j=1}^N \sigma(j) \quad (9)$$

where  $\sigma(j)$  is the atomic stress at atom  $j$  in the Z-direction and the  $J$  value is calculated using Equation (8).

### 2.3.2. Localized Deformation Zone

Micro-deformability can be reflected by the deformation field ahead of the crack-tip. In a non-hardening material which contains plastic deformation near a crack-tip, Rice et al. [42] considered that the deformation behavior is idealized as linear elastic until the

principal in-plane shear stress reaches a yield value and an elastic–plastic boundary cutting into the crack was assumed. The approximate characteristic size of the highly deformed zone or plastic zone ahead of the crack-tip can then be obtained as [46]:

$$R = \frac{3J}{4\sqrt{2}(1 + \pi/2)\sigma_y\epsilon_0} \quad (10)$$

where  $\sigma_y$  is the yield strength and  $\epsilon_0$  is the initial yield strain. Here,  $R$  is introduced to describe the deformability of the crack-tip field. Since in our single-crystal MD simulations, dislocations that are emitted from the crack-tip can move freely within the single crystal body, the calculated  $R$  from Equation (10), which corresponds to a localized deformation region, can be generally considered as a localized deformation zone size instead of a plastic zone size. With the growth of the applied load, the  $J$ -integral value increases, and then the localized deformation zone  $R$  becomes larger. When they reach the critical state, the crack-tip field becomes unstable and the crack propagates.

### 3. Results and Discussion

#### 3.1. Degree of Lattice Distortion and Chemical Short Range Order

To assess the magnitude of LD, we have measured the full width at half maximum (FWHM) of the radial distribution function  $g$  of the first nearest neighbor shell for different temperatures. The FWHM is estimated from a fit of  $g$  as a function of the interatomic distance  $r$  [39]. The comparison of the Random MEA with the average atomic sample enables a direct evaluation of the thermal shift from the inherent lattice distortion in MEAs. Figure 2a shows the FWHM as a function of the temperature  $T$ . The FWHM of the Ave-atom configuration represents thermal displacements. Moreover, the difference in FWHM between the Ave-atom configuration and Random configuration reveals the degree of LD. One can see that the increase in temperature leads to a monotonic increase in thermal displacements. However, the effect of lattice distortion decreases with the increase in temperature  $T$ ; in other words, LD can broaden  $g(r)$  most obviously at low temperatures.

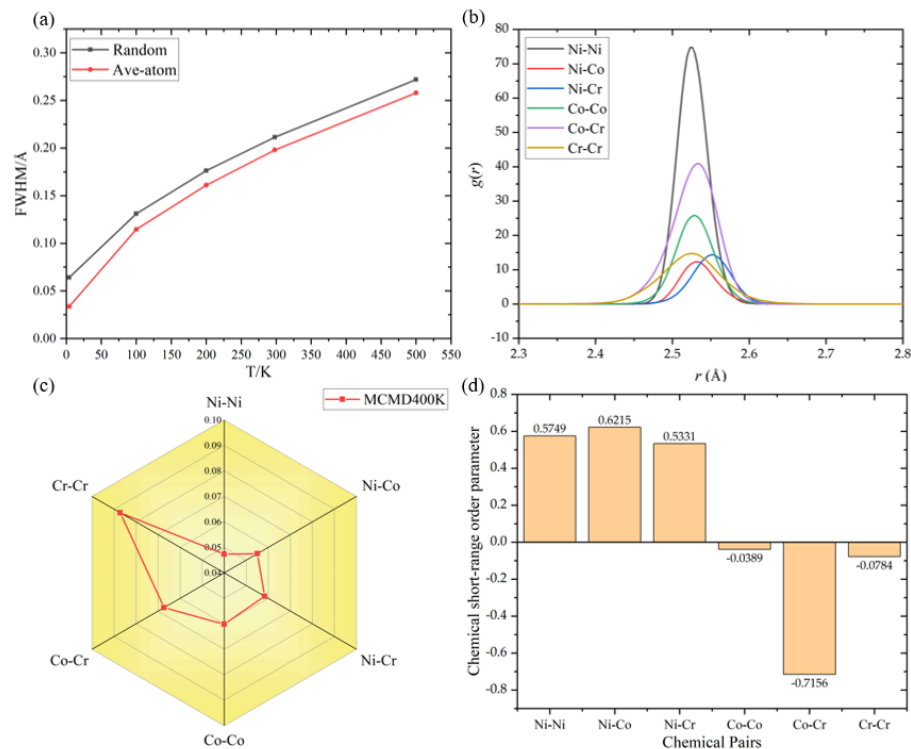


**Figure 2.** (a) shows the FWHM as a function of temperature for the Random MEA and the average atomic sample. The FWHM of the first nearest neighbor peak of  $g$  is taken as a measure for the intrinsic

lattice distortions in the MEA. A comparison of the Random sample and the Ave-atom sample reveals the degree of lattice distortion. (b) presents the radial distribution function  $g(r)$  of the MCMD400K configuration versus the interatomic distance  $r$  for different atomic pairs. (c) displays the FWHM of  $g(r)$  for different atomic pairs. (d) shows the result of the average CSRO parameter  $\alpha_{ij}^1$  for the MCMD400K CoCrNi MEA sample. Here, MCMD400K denotes the sample annealed at 400K during hybrid MD/MC simulations. Random and Ave-atom refer to configurations with an ideally uniform random atomic distribution and a mean-field model of the MEA produced by an A-atom potential, respectively.

In order to further understand the correlation between atomic pairs and LD, the  $g(r)$  and FWHM of various pairs for the MCMD400K configuration with CSRO and LD are shown in Figure 2b,c. Among these, we can see that Ni-Ni pairs possess the minimum FWHM and the highest peak of  $g(r)$ , indicating that the structural distortion is the minimum. This may result from the delocalized electronic behavior of Ni, which causes a small variation in the distance of Ni-Ni. On the contrary, Cr exhibits obvious local electronic behavior, which shows weak bonding ability, and leads to large changes in the distance of Cr-Cr [51], as manifested by large fluctuations in the distance of Cr-Cr, leading to a more considerable LD than Ni-Ni pair.

The CSRO parameter, which is also called the Warren–Cowley parameter, is usually used to characterize the degree of CSRO at the various annealed temperatures. The short-range order parameter ( $\alpha_{ij}$ ,  $i$  and  $j$  are Ni, Co or Cr) of each pair is defined as [32]

$$\alpha_{ij}^m = \frac{p_{ij}^m - C_j}{\delta_{ij} - C_j} \quad (11)$$

where  $m$  means the  $m_{\text{th}}$  nearest-neighbor shell of the atom  $i$ .  $p_{ij}^m$  is the average probability of finding a  $j$ -type atom around an  $i$ -type atom in the  $m_{\text{th}}$  shell,  $C_j$  is the average concentration of a  $j$ -type atom in the configuration and  $\delta_{ij}$  is the Kronecker delta. For pairs of the same species, a positive  $\alpha_{ij}^m$  suggests the tendency of segregation in the  $m_{\text{th}}$  shell, and a negative  $\alpha_{ij}^m$  means the opposite. On the contrary, for pairs of different elements, a negative  $\alpha_{ij}^m$  suggests the tendency of  $j$ -type clustering in the  $m_{\text{th}}$  shell of an  $i$ -type atom, while a positive  $\alpha_{ij}^m$  means the opposite [32]. A zero value of the CSRO parameter would describe a purely random solid solution.

In our study, preferential bonding between Co and Cr atoms and between Ni atoms can be seen visually in the MCMD400K configuration with CSRO in Figure 1. The CSRO in the final structure is quantified in Figure 2d according to the average CSRO parameter between the atomic pairs. On the one hand, the CSRO parameters of Ni-Ni and Co-Cr pairs are respectively large positive and negative values, indicating that there is a certain degree of clustering between these similar and different pairs [32]. The atomic bonds favored by energy will begin to form, thus reducing the overall energy of the system. On the other hand, CSRO parameters for the Ni-Co and Ni-Cr pairs are large positive values, indicating a tendency to avoid these different pairs. The CSRO values of Co-Co and Cr-Cr pairs are very small, which indicates that these element pairs lack CSRO.

### 3.2. Results of the J-Integral and Localized Deformation Zone Size

The stress–strain curve for three configurations is displayed in Figure 3a. It can be observed in Figure 3a that the MCMD400K and Ave-atom configurations have shown a higher yield strength as compared to the Random configuration.  $J$ -integral is introduced here to measure the driving force of crack growth, and it is calculated based on atomic data acquired by MD simulation. The calculated  $J$ -integrals for three configurations with different CSROs and LDs are shown in Figure 3b. Results show that the values of  $J$ -integrals under the same strain are different for considered configurations with different CSROs and LDs. The  $J$ -integral value of the MCMD400K configuration is the largest among the three configurations at the same strain. It reveals that the MCMD400K configuration

exhibits the largest crack driving force and is more inclined to crack propagation. On the contrary, the  $J$ -integral value of the Random configuration is the lowest, indicating the minimum crack driving force. This suggests that CSRO could be conducive to crack growth. We note that the  $J$ -integral value of Ave-atom MEA without LD is quite close to that of MCMD400K but higher than that of the Random sample with LD, implying that LD is beneficial to preventing crack growth. As is known, the value of the  $J$ -integral depends on both the strength and deformation. It was reported that CSRO can enhance the tensile strength due to the higher energy cost of moving a dislocation through or out of a high-value CSRO region [32]. This is consistent with the fact that the yield strength for MCMD400K is much higher than that of the others (Figure 3a). In the same way, based on the previous studies [38], LD lowers the Young's modulus and tensile strength (Figure 3a). These conform to the observed results that the MCMD400K and Random configurations show the largest and minimum  $J$ -integral values, respectively.

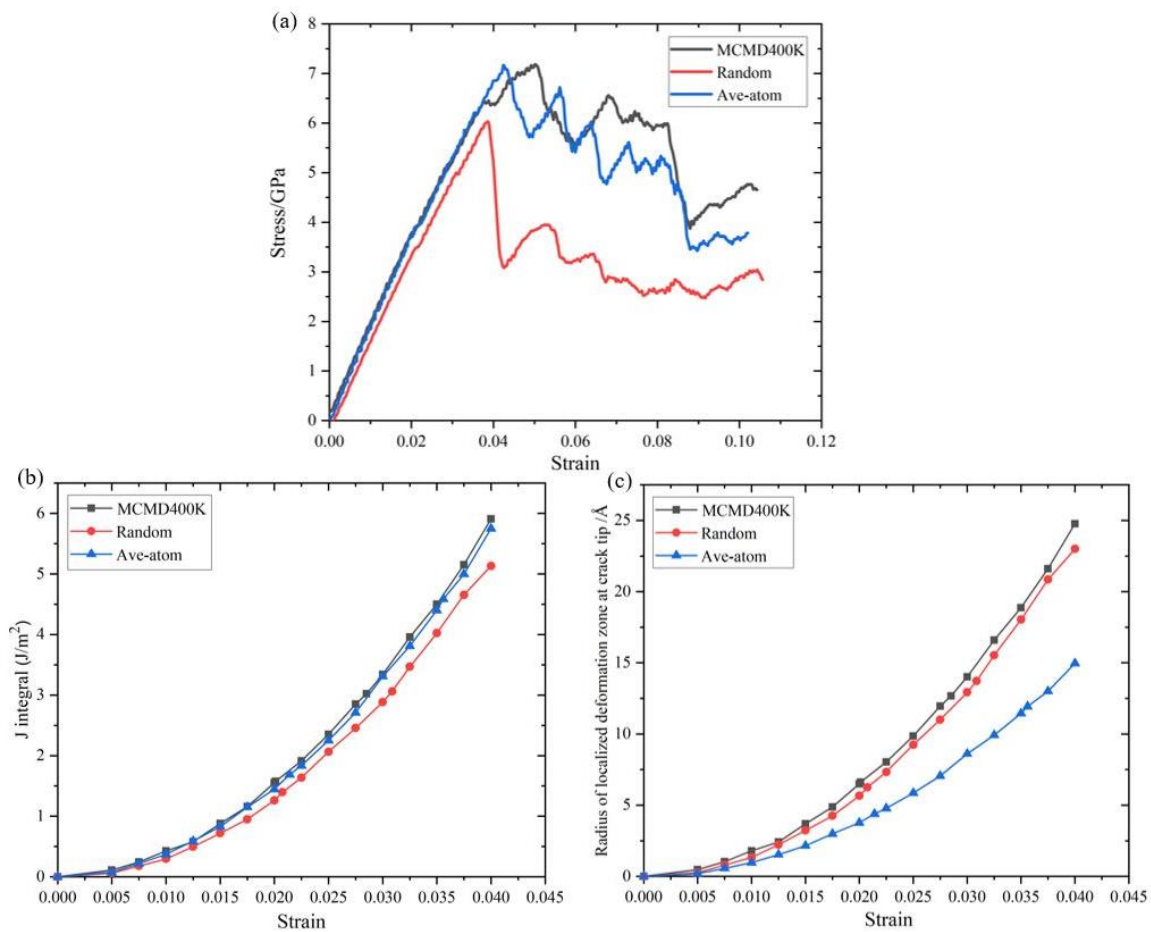


**Figure 3.** (a) The stress–strain curve for three configurations. (b) Evolution of the  $J$ -integrals with the strain for three configurations of different CSROs and LDs. (c) Radius of the localized deformation zone at the crack-tip versus the strain for three configurations. Here, the black, red and blue lines are, respectively, for the MCMD400K, Random and Ave-atom configurations.

The radius of the localized deformation zone at the crack-tip has been predicted based on Equation (10) for the considered three MEAs' configurations, and the results are shown in Figure 3c. We can see that the radius of the localized deformation zone for the MCMD400K configuration is the largest among the three configurations at the same strain, while the radius of the localized deformation zone of the Ave-atom configuration is the minimum. However, as is shown in Figure 3c, LD increases the localized deformation zone



size ahead of the crack-tip, indicating that the reason for the lower  $J$ -integral value of the random MEA is attributed to the sharp decrease in the tensile strength caused by LD.

### 3.3. Deformation Behavior and Mechanism of the Crack-Tip Field

To clearly understand the effect of CSRO and LD on the deformation evolution behavior of the crack-tip field, we analyze the evolution of the dislocation, twinning and phase transition ahead of the crack-tip at different strains for the MCMD400K, Random and Ave-atom configurations, respectively, as illustrated by Figure 4. Common Neighbor Analysis (CNA) in conjunction with a dislocation extraction algorithm (DXA) is employed to label each atom based on its local atomic coordination and gain the information of dislocations [60]. We can see that the deformation is governed by a synergy of stacking fault formation, especially dynamic recovery, dislocation, FCC-to-HCP phase transition and twinning.

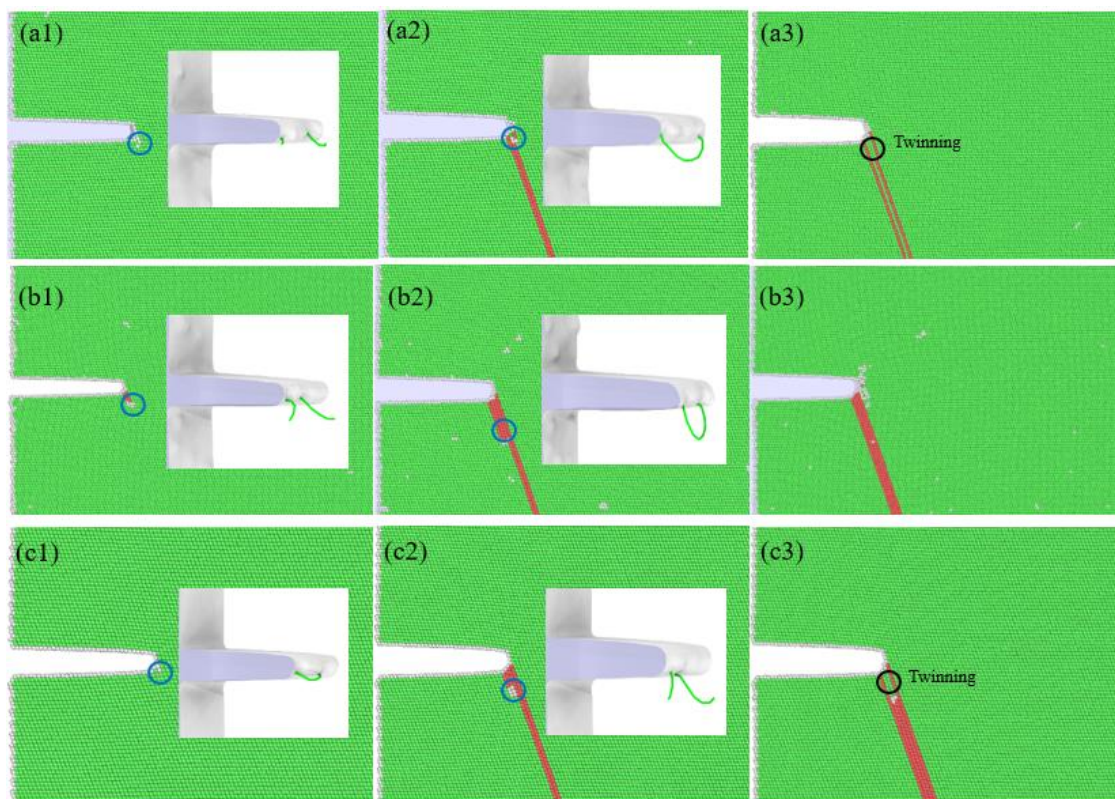


**Figure 4.** Shows the deformation evolution at the crack-tip for the MCMD400K configuration (a1–a3), Random configuration (b1–b3) and Ave-atom configuration (c1–c3), where the snapshots of the first, second and third dislocation nucleation and emission are given, respectively. Here, atoms are colored based on the common-neighbor analysis (CNA): white, red, blue and green atoms represent unknown, hexagonal-close-packed (hcp), body-centered-cubic (bcc) and face-centered-cubic (fcc) structures, respectively. The black circle region represents the twinning at the crack-tip. The blue circle area displays the DXA results at the crack-tip.

For the MCMD400K configuration with CSRO and LD, when the first leading partial dislocation is emitted (as shown in Figure 4(a1)), the strain is 0.0201 and the stress is 3.7 GPa. The  $J$ -integral value at this time is 1.577 J/m<sup>2</sup>. It can be seen that the stacking faults are formed and the deformation governing mechanism is dominated by dislocations emerging from the crack-tip at this time. When the strain increases to 0.0285 (as shown in Figure 4(a2)), the second leading partial dislocation is emitted. At this time, the  $J$ -integral value and the stress are 3.02 J/m<sup>2</sup> and 5.07 GPa, respectively. Subsequently, twinning begins to form. The nucleation of the second leading partial at the crack-tip and its glide on a slip plane adjacent

to the first leading partial dislocation act as the twinning source at the crack-tip. The plastic mechanism of the crack-tip region shifts to a combination of twinning and stacking faults. When the strain further increases to 0.0394 (as shown in Figure 4(a3)), the third leading partial dislocation is emitted. At this time, the  $J$ -integral value and the stress are 5.769 J/m<sup>2</sup> and 6.36 GPa, respectively. As the third leading partial dislocation slides along the slip plane adjacent to the previous dislocation, the number of twin layers increases. Based on the analysis above, the plastic deformation mechanism of the crack-tip field for the MCMD400K configuration is governed by a combination of twinning and stacking faults. It is proved by an experiment that the earlier onset of deformation nano-twinning is key to the exceptional damage-tolerance of this CrCoNi MEA [7].

For the Random configuration with LD but no CSRO, when the first leading partial dislocation is emitted (as shown in Figure 4(b1)), the strain is 0.0209 and the stress is 3.45 GPa. The  $J$ -integral value at this time is 1.395 J/m<sup>2</sup>. The stacking faults begin to form. When the strain increases to 0.031 (as shown in Figure 4(b2)), the second leading partial dislocation is emitted. At this time, the  $J$ -integral value and the stress are 3.02 J/m<sup>2</sup> and 5.07 GPa, respectively. The stacking faults transform to the HCP phase. The plasticity of the crack-tip region in Figure 4b is dominated by FCC-HCP phase transition. When the strain further increases to 0.0388 (as shown in Figure 4(b3)), the third leading partial dislocation is emitted. At this time, the  $J$ -integral value and the stress are 4.928 J/m<sup>2</sup> and 6.025 GPa, respectively. The continuous gliding of leading partial dislocation on the neighboring planes grows into the HCP phase. Note that dislocations of the phase transition glide on every other plane while twinning dislocations glide on successive slip planes, which leads to growth steps of two layers and one layer, respectively.

For the Ave-atom configuration without CSRO and LD, when the first leading partial dislocation is emitted (as shown in Figure 4(c1)), the strain is 0.0214. The  $J$ -integral value at this time is 1.686 J/m<sup>2</sup>. Subsequently, the Shockley leading partial dislocation begins to glide on the slip plane with the formation of stacking faults. When the strain increases to 0.0356 (as shown in Figure 4(c2)), the second leading partial dislocation is emitted. Owing to the stacking of intrinsic stacking faults, the HCP phases are formed. When the strain further increases to 0.041 (as shown in Figure 4(c3)), the third trailing partial dislocation is emitted. The HCP phase reduces due to the appearance of dynamic recovery. The continuous gliding of Shockley trailing partial dislocation overlaps the previous dislocation plane, and the middle atomic layer becomes faulted again, transforming back to FCC stacking. In this way, a twinning is formed. Thus, it can be seen that the crack-tip can be the source of FCC-HCP phase transition and twinning. The plastic deformation mechanism of the crack-tip region for the Ave-atom configuration is governed by a combination of FCC-HCP phase transition, stacking faults and twinning.

To sum up, CSRO can increase the critical strain for Shockley partial dislocation nucleation, and it makes twinning more pronounced. Compared to the Random structure without CSRO, the structure with CSRO is prone to resist the nucleation and glide of Shockley partial dislocations. As CSRO levels increase, the crack-tip is more likely to be surrounded by a single cluster, making it more difficult for Shockley partial dislocation to propagate from the nucleation site. In contrast, LD can lower the critical strain for Shockley partial dislocation nucleation, and it appears to encourage the nucleation of Shockley partial dislocations. Consequently, as shown in Figure 4b, the Random configuration with LD has more extensive dislocation motion near the crack-tip.

### 3.4. Stress-Dependent MEP of Dislocation Nucleation

We perform MEP calculations at different stress levels to collect sufficient data points because the activation energy varies with stress. The results of the activation energy barriers of three MEA configurations as a function of stress are shown in Figure 5. The dislocation activation energy decreases monotonically with the increase in stress, because the stress performs mechanical work to reduce the energy barrier. Note that the maximum energy at the saddle point on each MEP is defined as the activation energy under a specific stress.

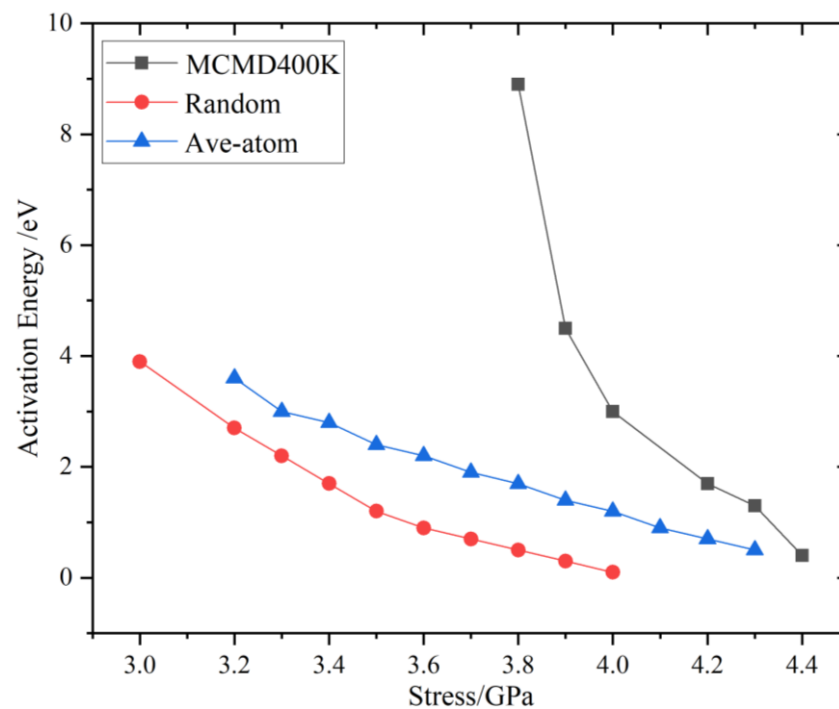


**Figure 5.** Stress-dependent activation energy for heterogeneous first Shockley partial dislocation nucleation. The activation energy is a function of the stress.

For the MCMD400K configuration with CSRO and LD, with increasing stress, the descent slope of the activation energy curve becomes smaller. In addition, the dislocation activation energy of the MCMD400K configuration is the largest among the three configurations at the same stress. Therefore, it is most difficult to nucleate dislocation. For the Random configuration with LD but no CSRO, the dislocation activation energy decreases from 3.9 to 0.1 eV when the stress increases from 3.0 to 4.0 GPa. With the increase in stress, the decrease in the dislocation activation energy is relatively gentle. The relatively low dislocation activation energy reveals that the Random configuration is more inclined to exhibit dislocation nucleation and emission. For the Ave-atom configuration without CSRO and LD, the dislocation activation energy changes more smoothly with the stress. Compared with the Random configuration, this configuration has a more difficult time performing dislocation nucleation and emission.

Consequently, the different effects of CSRO and LD on the yield strength, localized deformation zone and  $J$ -integral can be attributed to the distinct activation energy barrier and deformation mechanism. From the perspective of the activation energy barrier, CSRO can increase the Shockley partial dislocation activation energy barrier ahead of the crack-tip, leading to an enhancement in yield strength. In contrast, LD decreases the Shockley partial dislocation activation energy barrier from the crack-tip and causes a considerable reduction in yield strength. As shown in Figures 4 and 5, the activation energy barrier declines with increasing stress, accordingly, twinning or HCP phase transition appear due to the lower activation energy, as displayed in Figure 4. Furthermore, compared with those of Random and Ave-atom configurations, the Shockley partial dislocation activation energy barrier of the MCMD400K configuration is higher. HCP phase transition is found in the samples of the Random and Ave-atom configurations, which reveals that HCP phase transition may require a relatively low energy barrier (Figure 4). LD has a significant influence on the localized deformation zone size in Figure 3. LD can lower the critical strain for Shockley partial dislocation nucleation to increase the frequency of dislocation emission at the crack-tip, leading to a larger range of localized deformation zones at the crack-tip.

#### 4. Conclusions

In this work, we investigate the effects of CSRO and LD on the crack-tip behaviors and deformation mechanisms of CrCoNi MEAs under mode I loading at room temperature using molecular dynamics. Three types of MEA samples, namely, the MCMD400K, Random and Ave-atom configurations with different degrees of CSRO and LD, are built with a preexisting edge crack. The  $J$ -integral and the size of the localized deformation zone at the crack-tip are calculated to enable a quantitative understanding.

(1) The presence of CSRO can improve the  $J$ -integral value and yield strength significantly, but it hardly changes the localized deformation zone size. The presence of LD can lower the  $J$ -integral value and increase the size of the localized deformation zone considerably. LD causes a considerable reduction in yield strength.

(2) The deformation mechanism of the crack-tip region is governed by a combination of twinning, FCC-HCP phase transition and dislocation motion. Twinning from crack-tip is more prevalent in the MEAs with CSRO. The structure with CSRO is prone to resist the nucleation and glide of Shockley partial dislocations. LD can lower the critical strain for Shockley partial dislocation nucleation to increase the frequency of dislocation emission at the crack-tip, leading to a larger range of localized deformation zones at the crack-tip.

(3) LD lowers the activation energy barrier of Shockley partial dislocation from the crack-tip, while CSRO has the opposite effect, which serves as an underlying mechanism for the different effects of CSRO and LD on the yield strength,  $J$ -integral and localized deformation zone size.

**Author Contributions:** Conceptualization, Y.C.; Methodology, X.Z. and F.C.; Software, X.Z.; Validation, X.Z.; Formal analysis, X.Z.; Investigation, X.Z.; Resources, X.Z., F.C. and Y.C.; Data curation, X.Z.; Writing—original draft, X.Z.; Writing—review & editing, X.Z., F.C., L.D. and Y.C.; Visualization, X.Z.; Supervision, L.D. and Y.C.; Project administration, Y.C.; Funding acquisition, L.D. and Y.C. All authors have read and agreed to the published version of the manuscript.

**Funding:** This work is supported by the National Key Research and Development Program of China (No. 2022YFC3320504-02), the NSFC (Nos. 11972346, 12102433), the NSFC Basic Science Center Program for “Multi-scale Problems in Nonlinear Mechanics” (No.11988102), the Key Research Program of the Chinese Academy of Sciences (Grant No. ZDRW-CN-2021-2-3) and the opening project of State Key Laboratory of Explosion Science and Technology (Grant No. KFJJ23-03M).

**Data Availability Statement:** The data that support the findings of this study are available from the corresponding author upon reasonable request.

**Conflicts of Interest:** The authors declare no conflict of interest.

#### References

1. George, E.P.; Raabe, D.; Ritchie, R.O. High-entropy alloys. *Nat. Rev. Mater.* **2019**, *4*, 515–534. [[CrossRef](#)]
2. Yeh, J.W. Recent progress in high-entropy alloys. *Ann. Chim.-Sci. Mater.* **2006**, *31*, 633–648. [[CrossRef](#)]
3. Li, W.; Xie, D.; Li, D.; Zhang, Y.; Gao, Y.; Liaw, P.K. Mechanical behavior of high-entropy alloys. *Prog. Mater. Sci.* **2021**, *118*, 100777. [[CrossRef](#)]
4. Yang, X.G.; He, L.; Li, E.R.; Yang, C.L. Microstructure and Properties of Non-Equiatomic Ni<sub>10</sub>Cr<sub>6</sub>WFe<sub>9</sub>TiAl<sub>x</sub> High-Entropy Alloys Combined with High Strength and Toughness. *Metals* **2023**, *13*, 1179. [[CrossRef](#)]
5. Yi, H.L.; Bi, M.Y.; Yang, K.; Zhang, B. Significant Improvement the Mechanical Properties of CoCrNi Alloy by Tailoring a Dual FCC-Phase Structure. *Materials* **2020**, *13*, 4909. [[CrossRef](#)] [[PubMed](#)]
6. Gludovatz, B.; Hohenwarter, A.; Catoor, D.; Chang, E.H.; George, E.P.; Ritchie, R.O. A fracture-resistant high-entropy alloy for cryogenic applications. *Science* **2014**, *345*, 1153–1158. [[CrossRef](#)] [[PubMed](#)]
7. Gludovatz, B.; Hohenwarter, A.; Thurston, K.V.S.; Bei, H.B.; Wu, Z.G.; George, E.P.; Ritchie, R.O. Exceptional damage-tolerance of a medium-entropy alloy CrCoNi at cryogenic temperatures. *Nat. Commun.* **2016**, *7*, 10602. [[CrossRef](#)]
8. Liu, Z.Q.; Shi, X.H.; Zhang, M.; Qiao, J.W. Development of Refractory High Entropy Alloys with Tensile Ductility at Room Temperature. *Metals* **2023**, *13*, 329. [[CrossRef](#)]
9. Qiu, X.W.; Zhang, Y.P.; He, L.; Liu, C.G. Microstructure and corrosion resistance of AlCrFeCuCo high entropy alloy. *J. Alloys Compd.* **2013**, *549*, 195–199. [[CrossRef](#)]
10. Li, T.R.; Wang, D.B.; Zhang, S.D.; Wang, J.Q. Corrosion Behavior of High Entropy Alloys and Their Application in the Nuclear Industry-An Overview. *Metals* **2023**, *13*, 363. [[CrossRef](#)]

11. Luo, H.; Sohn, S.S.; Lu, W.J.; Li, L.L.; Li, X.G.; Soundararajan, C.K.; Krieger, W.; Li, Z.M.; Raabe, D. A strong and ductile medium-entropy alloy resists hydrogen embrittlement and corrosion. *Nat. Commun.* **2020**, *11*, 3081. [[CrossRef](#)]
12. Lu, K.; Zhu, J.; Guo, D.; Yang, M.; Sun, H.; Wang, Z.; Hui, X.; Wu, Y. Microstructures, Corrosion Resistance and Wear Resistance of High-Entropy Alloys Coatings with Various Compositions Prepared by Laser Cladding: A Review. *Coatings* **2022**, *12*, 1023. [[CrossRef](#)]
13. Kołodziejczak, P.; Bober, M.; Chmielewski, T. Wear Resistance Comparison Research of High-Alloy Protective Coatings for Power Industry Prepared by Means of CMT Cladding. *Appl. Sci.* **2022**, *12*, 4568. [[CrossRef](#)]
14. Liu, X.F.; Tian, Z.L.; Zhang, X.F.; Chen, H.H.; Liu, T.W.; Chen, Y.; Wang, Y.J.; Dai, L.H. “Self-sharpening” tungsten high-entropy alloy. *Acta Mater.* **2020**, *186*, 257–266. [[CrossRef](#)]
15. Wu, Z.; Bei, H.; Pharr, G.M.; George, E.P. Temperature dependence of the mechanical properties of equiatomic solid solution alloys with face-centered cubic crystal structures. *Acta Mater.* **2014**, *81*, 428–441. [[CrossRef](#)]
16. Zhao, Y.L.; Yang, T.; Tong, Y.; Wang, J.; Luan, J.H.; Jiao, Z.B.; Chen, D.; Yang, Y.; Hu, A.; Liu, C.T.; et al. Heterogeneous precipitation behavior and stacking-fault-mediated deformation in a CoCrNi-based medium-entropy alloy. *Acta Mater.* **2017**, *138*, 72–82. [[CrossRef](#)]
17. Li, X.T.; Sheinerman, A.G.; Yang, H.; Zhu, Z.Y. Theoretical modeling of toughening mechanisms in the CrMnFeCoNi high-entropy alloy at room temperature. *Int. J. Plast.* **2022**, *154*, 103304. [[CrossRef](#)]
18. Li, J.; Chen, H.T.; He, Q.F.; Fang, Q.H.; Liu, B.; Jiang, C.; Liu, Y.; Yang, Y.; Liaw, P.K. Unveiling the atomic-scale origins of high damage tolerance of single-crystal high entropy alloys. *Phys. Rev. Mater.* **2020**, *4*, 103612. [[CrossRef](#)]
19. Singh, S.K.; Parashar, A. Atomistic simulations to study crack tip behaviour in multi-elemental alloys. *Eng. Fract. Mech.* **2021**, *243*, 107536. [[CrossRef](#)]
20. Kim, S.W.; Kim, J.H. In-situ observations of deformation twins and crack propagation in a CoCrFeNiMn high-entropy alloy. *Mater. Sci. Eng. A* **2018**, *718*, 321–325. [[CrossRef](#)]
21. Li, X.T.; Jiang, X.Y. Theoretical analyses of nanocrack nucleation near the main crack tip in nano and micro crystalline materials. *Eng. Fract. Mech.* **2019**, *221*, 106672. [[CrossRef](#)]
22. Clement, N.; Caillard, D.; Martin, J.L. Heterogeneous deformation of concentrated Ni-Cr FCC alloys—Macroscopic and microscopic behavior. *Acta Mater.* **1984**, *32*, 961–975. [[CrossRef](#)]
23. Dubiel, S.M.; Cieslak, J. Short-range order in iron-rich Fe-Cr alloys as revealed by Mossbauer spectroscopy. *Phys. Rev. B* **2011**, *83*, 180202. [[CrossRef](#)]
24. Owen, L.R.; Playford, H.Y.; Stone, H.J.; Tucker, M.G. Analysis of short-range order in Cu<sub>3</sub>Au using X-ray pair distribution functions. *Acta Mater.* **2017**, *125*, 15–26. [[CrossRef](#)]
25. Schonfeld, B. Local atomic arrangements in binary alloys. *Prog. Mater. Sci.* **1999**, *44*, 435–543. [[CrossRef](#)]
26. Santodonato, L.J.; Zhang, Y.; Feygenson, M.; Parish, C.M.; Gao, M.C.; Weber, R.J.K.; Neufeind, J.C.; Tang, Z.; Liaw, P.K. Deviation from high-entropy configurations in the atomic distributions of a multi-principal-element alloy. *Nat. Commun.* **2015**, *6*, 5964. [[CrossRef](#)]
27. Singh, P.; Smirnov, A.V.; Johnson, D.D. Atomic short-range order and incipient long-range order in high-entropy alloys. *Phys. Rev. B* **2015**, *91*, 224204. [[CrossRef](#)]
28. Tamm, A.; Aabloo, A.; Klintonberg, M.; Stocks, M.; Caro, A. Atomic-scale properties of Ni-based FCC ternary, and quaternary alloys. *Acta Mater.* **2015**, *99*, 307–312. [[CrossRef](#)]
29. Chen, X.F.; Wang, Q.; Cheng, Z.Y.; Zhu, M.L.; Zhou, H.; Jiang, P.; Zhou, L.L.; Xue, Q.Q.; Yuan, F.P.; Zhu, J.; et al. Direct observation of chemical short-range order in a medium-entropy alloy. *Nature* **2021**, *592*, 712–716. [[CrossRef](#)]
30. Zhou, L.L.; Wang, Q.; Wang, J.; Chen, X.F.; Jiang, P.; Zhou, H.; Yuan, F.P.; Wu, X.L.; Cheng, Z.Y.; Ma, E. Atomic-scale evidence of chemical short-range order in CrCoNi medium-entropy alloy. *Acta Mater.* **2022**, *224*, 117490. [[CrossRef](#)]
31. Ding, J.; Yu, Q.; Asta, M.; Ritchie, R.O. Tunable stacking fault energies by tailoring local chemical order in CrCoNi medium-entropy alloys. *Proc. Natl. Acad. Sci. USA* **2018**, *115*, 8919–8924. [[CrossRef](#)]
32. Li, Q.J.; Sheng, H.; Ma, E. Strengthening in multi-principal element alloys with local-chemical-order roughened dislocation pathways. *Nat. Commun.* **2019**, *10*, 3563. [[CrossRef](#)]
33. Han, D.; Wang, Z.Y.; Yan, Y.; Shi, F.; Li, X.W. A good strength-ductility match in Cu-Mn alloys with high stacking fault energies: Determinant effect of short range ordering. *Scr. Mater.* **2017**, *133*, 59–64. [[CrossRef](#)]
34. Zhang, Y.J.; Han, D.; Li, X.W. A unique two-stage strength-ductility match in low solid-solution hardening Ni-Cr alloys: Decisive role of short range ordering. *Scr. Mater.* **2020**, *178*, 269–273. [[CrossRef](#)]
35. Zhang, R.P.; Zhao, S.T.; Ding, J.; Chong, Y.; Jia, T.; Ophus, C.; Asta, M.; Ritchie, R.O.; Minor, A.M. Short-range order and its impact on the CrCoNi medium-entropy alloy. *Nature* **2020**, *581*, 283–287. [[CrossRef](#)]
36. Ghosh, S.; Sotnikov, V.; Shapeev, A.V.; Neugebauer, J.; Körmann, F. Short-range order and phase stability of CrCoNi explored with machine learning potentials. *Phys. Rev. Mater.* **2022**, *6*, 113804. [[CrossRef](#)]
37. Lee, C.; Song, G.; Gao, M.C.; Feng, R.; Chen, P.Y.; Brechtel, J.; Chen, Y.; An, K.; Guo, W.; Poplawsky, J.D.; et al. Lattice distortion in a strong and ductile refractory high-entropy alloy. *Acta Mater.* **2018**, *160*, 158–172. [[CrossRef](#)]
38. Jian, W.R.; Xie, Z.C.; Xu, S.Z.; Su, Y.Q.; Yao, X.H.; Beyerlein, I.J. Effects of lattice distortion and chemical short-range order on the mechanisms of deformation in medium entropy alloy CoCrNi. *Acta Mater.* **2020**, *199*, 352–369. [[CrossRef](#)]

39. Utt, D.; Stukowski, A.; Albe, K. Grain boundary structure and mobility in high-entropy alloys: A comparative molecular dynamics study on a Sigma 11 symmetrical tilt grain boundary in face-centered cubic CuNiCoFe. *Acta Mater.* **2020**, *186*, 11–19. [[CrossRef](#)]
40. Peng, W.; Yuan, W.; Jiabin, L.; Hongtao, W. Impacts of atomic scale lattice distortion on dislocation activity in high-entropy alloys. *Extrem. Mech. Lett.* **2017**, *17*, 38–42.
41. Bahramyan, M.; Mousavian, R.T.; Brabazon, D. Determination of atomic-scale structure and compressive behavior of solidified AlxCrCoFeCuNi high entropy alloys. *Int. J. Mech. Sci.* **2020**, *171*, 105389. [[CrossRef](#)]
42. Bahramyan, M.; Mousavian, R.T.; Brabazon, D. Study of the plastic deformation mechanism of TRIP-TWIP high entropy alloys at the atomic level. *Int. J. Plast.* **2020**, *127*, 102649. [[CrossRef](#)]
43. Afkham, Y.; Bahramyan, M.; Mousavian, R.T.; Brabazon, D. Tensile properties of AlCrCoFeCuNi glassy alloys: A molecular dynamics simulation study. *Mater. Sci. Eng. A* **2017**, *698*, 143–151. [[CrossRef](#)]
44. Zhou, L.; Guo, Y.F. Dislocation-Governed Plastic Deformation and Fracture Toughness of Nanotwinned Magnesium. *Materials* **2015**, *8*, 5250–5264. [[CrossRef](#)]
45. Cao, F.H.; Chen, Y.; Wang, H.Y.; Dai, L.H. Chemical inhomogeneity inhibits grain boundary fracture: A comparative study in CrCoNi medium entropy alloy. *J. Mater. Sci. Technol.* **2023**, *153*, 228–241. [[CrossRef](#)]
46. Rice, J.R. A Path Independent Integral and the Approximate Analysis of Strain Concentration by Notches and Cracks. *J. Appl. Mech.* **1968**, *35*, 379–386. [[CrossRef](#)]
47. Shih, C.F. Relationships between the J-integral and the crack opening displacement for stationary and extending cracks. *J. Mech. Phys. Solids* **1981**, *29*, 305–326. [[CrossRef](#)]
48. Roy, S.; Roy, A. A computational investigation of length-scale effects in the fracture behaviour of a graphene sheet using the atomistic J-integral. *Eng. Fract. Mech.* **2019**, *207*, 165–180. [[CrossRef](#)]
49. Chowdhury, S.C.; Wise, E.A.; Ganesh, R.; Gillespie, J.W. Effects of surface crack on the mechanical properties of Silica: A molecular dynamics simulation study. *Eng. Fract. Mech.* **2019**, *207*, 99–108. [[CrossRef](#)]
50. Ji, W.M.; Wu, M.S. Atomistic studies of ductile fracture of a single crystalline cantor alloy containing a crack at cryogenic temperatures. *Eng. Fract. Mech.* **2021**, *258*, 108120. [[CrossRef](#)]
51. Cao, F.H.; Chen, Y.; Zhao, S.T.; Ma, E.; Dai, L.H. Grain boundary phase transformation in a CrCoNi complex concentrated alloy. *Acta Mater.* **2021**, *209*, 116786. [[CrossRef](#)]
52. Nosé, S. A molecular dynamics method for simulations in the canonical ensemble. *Mol. Phys.* **1984**, *52*, 255–268. [[CrossRef](#)]
53. Hoover, W.G. Canonical dynamics: Equilibrium phase-space distributions. *Phys. Rev. A* **1985**, *31*, 1695–1697. [[CrossRef](#)]
54. Stukowski, A. Visualization and analysis of atomistic simulation data with OVITO—the Open Visualization Tool. *Modell. Simul. Mater. Sci. Eng.* **2010**, *18*, 015012. [[CrossRef](#)]
55. Cao, F.H.; Wang, Y.J.; Dai, L.H. Novel atomic-scale mechanism of incipient plasticity in a chemically complex CrCoNi medium-entropy alloy associated with inhomogeneity in local chemical environment. *Acta Mater.* **2020**, *194*, 283–294. [[CrossRef](#)]
56. Zhang, J.Y.; Zhang, H.W.; Ye, H.F.; Zheng, Y.G. Free-end adaptive nudged elastic band method for locating transition states in minimum energy path calculation. *J. Chem. Phys.* **2016**, *145*, 094104. [[CrossRef](#)]
57. Zhu, T.; Li, J.; Samanta, A.; Kim, H.G.; Suresh, S. Interfacial plasticity governs strain rate sensitivity and ductility in nanostructured metals. *Proc. Natl. Acad. Sci. USA* **2007**, *104*, 3031–3036. [[CrossRef](#)]
58. Liang, L.W.; Dai, S.C.; Chen, Y.; Wang, H.Y.; Wang, Y.J.; Dai, L.H. Emergent failure transition of pearlitic steel at extremely high strain rates. *Comput. Mater. Sci.* **2023**, *219*, 112005. [[CrossRef](#)]
59. Krull, H.; Yuan, H.A. Suggestions to the cohesive traction-separation law from atomistic simulations. *Eng. Fract. Mech.* **2011**, *78*, 525–533. [[CrossRef](#)]
60. Ji, W.M.; Wu, M.S. Nanoscale insights into the damage tolerance of Cantor alloys at cryogenic temperatures. *Int. J. Mech. Sci.* **2022**, *226*, 107406. [[CrossRef](#)]

**Disclaimer/Publisher’s Note:** The statements, opinions and data contained in all publications are solely those of the individual author(s) and contributor(s) and not of MDPI and/or the editor(s). MDPI and/or the editor(s) disclaim responsibility for any injury to people or property resulting from any ideas, methods, instructions or products referred to in the content.